Research Square

Preprints are preliminary reports that have not undergone peer review.
They should not be considered conclusive, used to inform clinical practice,
or referenced by the media as validated information.

Synthesis, Characterization, Molecular docking, Molecular simulation, DFT and Anti-Infective Efficacy of Chromen-4-one Derivative

Vinoth M

vinobioinfo@gmail.com

IFET College of Engineering

Kodisundaram P

Dhandapai A

Kumar K.M

Research Article

Keywords: Acacia nilotica, NMR, Mass spectrometry, chromen-4-one, biological activity, HEpG cell lines

Posted Date: October 29th, 2026

DOI: https://doi.org/10.21203/rs.3.rs-11226850/v1

License: This work is licensed under a Creative Commons Attribution 4.0 International License.
Read Full License

Additional Declarations: No competing interests reported.

Synthesis, Characterization, Molecular docking, Molecular simulation, DFT and Anti-Infective Efficacy of Chromen-4-one Derivative

M.Vinoth[a*], P. Kodisundaram[b], A.Dhandapai[c], K.M Kumar [d],

[a*]Department of Chemistry, IFET Engineering College (Autonomous), Villupuram, 605108, Tamil Nadu. India. *vinobioinfo@gmail.com*

[b]Department of Surgery, Miller School of Medicine, University of Miami, FL 33136, USA. *kxp641@miami.edu*

[c]Department of Chemistry, C.K.College of Engineering &Technology, Cuddalore, 607003, Tamil Nadu India. *dhana118msc@gmail.com*

[d]Department of Bioinformatics, Pondicherry University, Puducherry 605014, kumarkm@bicpu.edu.in

[*]Authors to whom correspondence should be addressed.

Abstract: *Acacia nilotica,* commonly known as the *Nile acacia*, is a weedy tropical plant with several medicinally active secondary metabolites. Chromen-4-one derivative, 8-allyl-2-(3-hydroxyphenyl)-4H-chromen-4-one compound, was isolated by methanol extract from the leaves of Acacia nilotica and characterized using various spectral analyses (FTIR, 1 & 2D NMR), as well as by mass spectrometry. Further, two different concentrations of methanol extract (50mg/ml and 100 mg/ml) were screened for its biological activity against fungal and bacterial infection (gram-negative and gram-positive organisms). The results were compared with standard ampicillin and fluconazole. Our results show that ethanol extract from leaves *Acacia nilotica* possesses significant antibacterial, MIC, and antifungal activities. The isolated compound also showed potent anticancer efficacy against HEpG tumor cell lines. These findings underscore the potential therapeutic benefit of *Acacia nilotica* extracts for fungal and bacterial infections. Additional DFT studies yield two top-hit compounds via frontier molecular orbitals for structural stability and reactivity analysis. Following the molecular docking and molecular simulation analysis revealed a potential inhibitor for, cancer protein 8I0L receptor. Thus, our study will make a landmark treatment option for infections, not only for fungal and bacterial infections but also can be extended to other infectious diseases.

Keywords: *Acacia nilotica, NMR, Mass spectrometry, chromen-4-one, biological activity, HEpG cell lines.*

1. Introduction

Acacia nilotica, commonly known as Nile acacia, is a tropical plant with global distribution and notable medicinal properties attributed to the chemical constituents present in its leaves. Recent investigations have emphasized its role in traditional healing practices, prompting further exploration into its potential clinical applications [1, 2]. This paper provides a comprehensive overview of the phytochemical composition of *Acacia nilotica*, focusing on alkaloids, flavonoids, tannins, and chromenone derivatives, along with their associated biological activities, including anti-inflammatory, anticancer, antibacterial, and antioxidant effects [3,4]. Moreover, we outline the analytical methodologies employed for structural elucidation and the extraction techniques for isolating bioactive compounds from *Acacia nilotica* leaves. This in-depth analysis highlights the potential of *Acacia nilotica* as a reservoir of pharmacologically relevant natural compounds while also suggesting avenues for future research to harness its medicinal benefits further [5,6]. Of particular interest are chromenone derivatives, well-known for their pharmacological significance, encompassing anti-inflammatory, antioxidant, anticancer, and antibacterial properties. The investigation into the biological evaluation, structural characterization, and isolation of chromenone derivatives from Acacia nilotica leaves underscores their considerable promise, aligning with the burgeoning interest in novel medicinal agents from other natural reservoirs [7-10]. This study aims to extract specific chromenone derivatives from *Acacia nilotica* leaves, employ modern spectroscopic and chromatographic techniques for structural elucidation, and assess their potential biological activities [11-14]. By delineating these molecules' chemical profile and pharmacological potential, this research is intended to foster future inquiry and discovery of new drug leads or therapeutic agents derived from natural origins [15,16].Furthermore, exploring the therapeutic attributes of *Acacia nilotica* leaves may provide insights into their traditional folk medicine uses and cultivate the development of additional evidence-based alternative therapies [17,18].

2. Materials and Methods

2.1 *Spectral Analysis*

The FT–IR spectrum of the synthesized compound was obtained using a Shimadzu FT–IR spectrometer by preparing the sample in KBr pellets, and the spectra were recorded in the range of 4000–400 cm^{-1}. The ^{1}H NMR (500 MHz) and ^{13}C NMR (125 MHz) spectra were measured on a Bruker Avance II 500 NMR spectrometer using 5 mm NMR tubes. Deuterated chloroform ($CDCl_3$) was used as the solvent, while tetramethylsilane (TMS) served as the internal reference standard, and the chemical shifts were expressed in δ (ppm). The DEPT-135 experiment was performed using a conventional 135° pulse sequence in order to distinguish CH, CH_2, and CH_3 carbon signals. In addition, two-dimensional NMR experiments such as ^{1}H–^{1}H COSY and HSQC were carried out using standard Bruker pulse programs to study proton–proton and proton–carbon correlations within the molecule. The mass spectrum of the compound was recorded using a Micromass Q-TOF mass spectrometer equipped with a data acquisition system. This instrument operates as a high-resolution double-focusing mass analyzer, providing a maximum resolution of approximately 6000 and a calibrated mass range up to 1500 Da. The analysis was performed using electron impact (EI) and chemical ionization (CI) modes as the ionization sources [19,20].

2.2 *Antifungal assay*

The antifungal activity of the methanol extract of Acacia nilotica leaves was evaluated by inoculating fungal isolates on Sabouraud's Dextrose Agar (SDA) plates and incubating them at 28°C for three to five days. Before inoculation, SDA plates were sterilized, and wells were created in the agar using a sterile cork borer (6 mm in diameter). A fungal disc was placed in the central well, while each

peripheral well-received 50 µL of the extract(s). To serve as a negative control, sterilized dimethyl sulfoxide (DMSO) was added to one of the peripheral wells. The plates were then incubated at 28°C. Colon diameter measurements were taken daily, starting 24 hours after the experiment commenced and concluding when the fungus had covered two-thirds of the control treatment's plate surface. Zones of inhibition were indicative of the antibacterial activity of the test material. Each experiment was conducted in triplicate [21-23].

2.3 Assessment of minimum inhibitory concentration (MIC)

The agar-well diffusion method determined the crude extract's minimum inhibitory concentration (MIC). The test extract was initially dissolved in dimethyl sulfoxide (DMSO) for a twofold serial dilution. Subsequently, sterile DMSO was utilized to dilute the extract to concentrations ranging from 1000 to 31.25 mg/mL. Each dilution was aseptically applied in 50 µL volumes onto Mueller Hinton agar plates previously inoculated with a standardized bacterial inoculum (106 CFU/mL). Sodium propionate served as the positive control in this experiment. Each assay was replicated three times. A similar procedure was adopted for fungi, except Sabouraud's Dextrose Agar (SDA) plates were used and incubated at 28°C [24,25].

2.4 Cytotoxicity assay

The MTT assay was performed using 3-(4,5-dimethylthiazol-2-yl)-2,5-diphenyl tetrazolium bromide to determine cell viability. In living cells, mitochondrial enzymes such as succinate dehydrogenase and reductase reduce MTT to an insoluble purple formazan product. The quantity of formazan formed is directly related to the number of metabolically active cells and decreases with increasing cytotoxic effects. After 48 hours of incubation, MTT solution was added to each well and the plates were kept at room temperature for 3 hours to allow formazan formation. After incubation, 100 µL of SDS dissolved in DMSO was added to each well to solubilize the resulting formazan crystals. Finally, the absorbance was recorded at 570 nm using a ReadWell Touch microplate reader to determine cell viability [26,27].

2.5 Frontier Molecular Orbital analysis

The energy separation between the highest occupied molecular orbital (HOMO) and the lowest unoccupied molecular orbital (LUMO) is an important parameter for understanding the chemical behavior of molecules. A smaller HOMO–LUMO gap generally indicates higher chemical reactivity and lower kinetic stability, and such systems are commonly described as soft molecules [28]. In this study, quantum chemical calculations were performed using the Gaussian 09 program package. The calculations were carried out within the framework of Density Functional Theory (DFT) using the B3LYP exchange–correlation functional together with the LanL2DZ basis set, which includes the Los Alamos National Laboratory double-zeta effective core potential (ECP). The molecular geometries of the selected compounds were first optimized to obtain their stable structures. After optimization, the electronic properties and stability of the molecules were further investigated through frontier molecular orbital (FMO) and molecular electrostatic potential (MEP) analyses. The spatial distributions of the HOMO and LUMO orbitals, as well as the electrostatic potential surface maps, were visualized with the GaussView 05 software package [29,30].

2.6 Protein structure modelling and molecular docking

The FASTA sequence of the target protein, Cyclin-dependent kinase 9 (CDK9), was obtained from the UniProt database. The SWISS-MODEL server was used to model the target protein. The top 3D protein model was selected based on the global model quality estimate (GMQE) score. Molecular docking was performed using AutoDock Vina to study the binding mode of the 8-allyl-2-(3-hydroxyphenyl)-4H-chromen-4-one compound in the CDK9 model. Receptor and ligand preparation

were performed using AutoDock Tools (ATD) 1.5.7 (https://ccsb.scripps.edu/mgltools/downloads/), and a grid box was set on the active site region. Finally, the 8-allyl-2-(3-hydroxyphenyl)-4H-chromen-4-one compound was docked into the active site of the CDK9 model to calculate its binding affinity. The biomolecular visualization of the 3D interaction of the compound was conducted using PyMOL [30-31].

2.7 Protein-ligand complex simulation

The Molecular Dynamics Simulation was performed 8-allyl-2-(3-hydroxyphenyl)-4H-chromen-4-one- CDK9 protein complex by using GROMACS version in the 2023.4 series with the CHARMM27 all–atom force field (CHARM22 plus CMAP for proteins) [32,33]. The protein-ligand complex was simulated for the period of 100 nano second (ns). This complex was solvated by using the water model TIP3P. A dodecahedral simulation box with a size of 1.0 nm (10 Å) was employed to facilitate unrestricted molecular dynamics of the complex and CL^- ions were added to neutralize net charge, stabilize biomolecular structures of the system [34–35]. Now the modeled structure is from the short steric clashes by using the steepest energy minimization. The complex structure was equilibrated with restraint constats are set to 1000 kj/mol/nm^2 for each direction (x, y, z) under the NVT and NPT ensemble. The protein–ligand complex stability during the molecular dynamics simulation was examined by calculating RMSD, RMSF, radius of gyration (Rg), and hydrogen bonding interactions using the GROMACS simulation package [36–38].

3. Results and Discussion

3.1 FTIR

The spectral analysis of the chromen-4-one derivative compound 4 is depicted in Figure 1, with the functional group peaks summarized in Figure 1. Notably, a prominent peak at 3447 cm-1 indicates the stretching vibration of the hydroxyl functional group. Additionally, peaks corresponding to aromatic and aliphatic C-H stretching frequencies were observed within the 3002, 2955, and 2921 cm-1 range. The stretching vibrations of carbonyl and alkyl ether groups were discerned at 1712 and 1654 cm-1, respectively. Furthermore, C-H bending vibrations were evident at 1418 cm-1, while hydroxyl (OH) bending vibrations were observed at 1330 cm-1. These findings suggest the presence of hydroxyl (OH) and C-H vibrations associated with flavonoid and phenolic compounds.

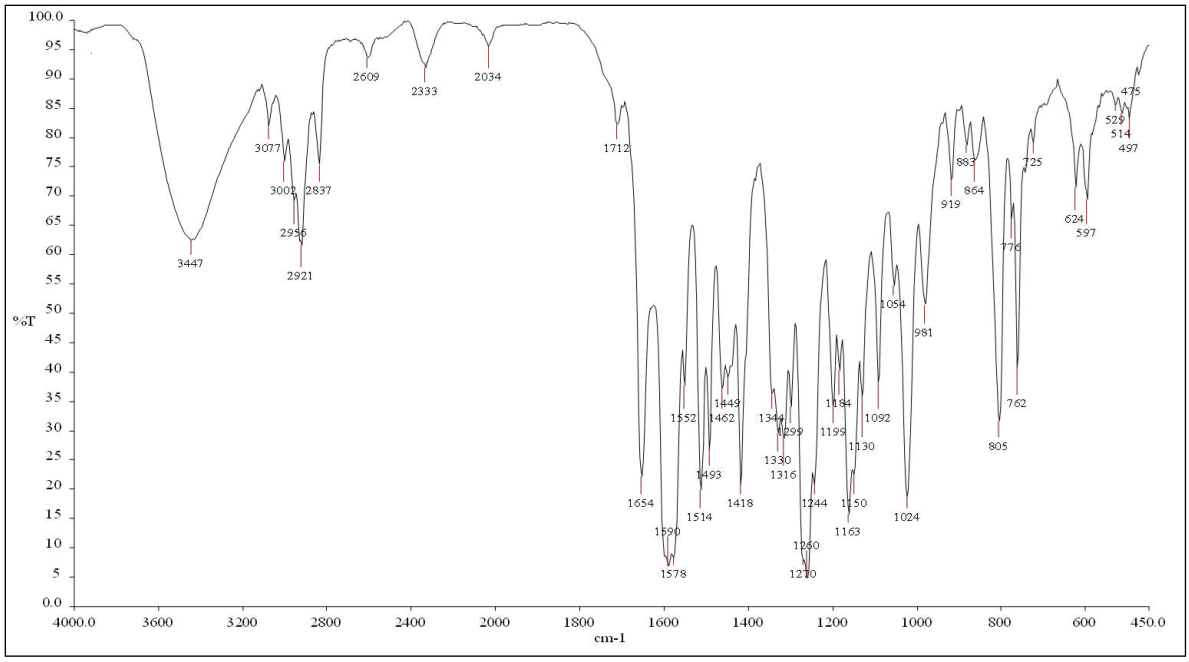


FIG: 1 spectral analysis of the chromen-4-one derivative compound 4

Table 1 FT-IR Spectral Analysis- chromen-4-one derivative

Peak Wavenumber cm^{-1}	Vibration Type	Functional Groups
3447	-O-H (stret)	Alcohol
3002,2955,2921	-C-H (Ar stret)	Aliphatic, Aromatic
2837	-C-H (Sp^3 stret)	Methylene
1712	-C=O (stret)	Carbonyl
1654	-C=C (stret)	Alkyl Ether
1418	-C-H (bend)	Aromatic
1330	-O-H (bend)	Alcohol

3.2 NMR 1D and 2D

The structural elucidation of the chromen-4-one motif-containing product demonstrated the presence of three rings labeled A, C, and B, as illustrated in Figure 2. This elucidation involves comprehensive chemical characterization, including the assignment of chemical shifts and coupling constants, facilitated by the combined application of 1H and 13C nuclear magnetic resonance (NMR), mainly through 1D and 2D NMR techniques such as COSY and HSQC.

Analysis of the NMR spectra of the compound reveals corresponding chemical shift values spanning the range of δ 3.56 - 7.64 ppm. Various proton environments are evident in the 1H NMR

spectrum (Figure 3a). Interestingly, a doublet peak at δ 3.56 ppm corresponds to aliphatic -CH2- methylene protons and a multiplet peak at δ 4.92-4.82 ppm indicates alkene -CH2 protons. The allyl -CH (methine proton) also manifests as a multiplet at δ 5.75-5.68 ppm. A singlet peak observed at δ 6.71 ppm corresponds to =CH (ring C, C3 comprising methine proton), whereas a doublet of doublet peak at δ 6.98 ppm corresponds to =CH proton at the C2' position. Methine protons at C4', C5', and C6' positions of ring B are observed at 6.81, 7.14, and 6.76 ppm, respectively. Similarly, aromatic proton peaks within ring. A exhibit a doublet at 7.64 ppm for C5 position, a triplet at 7.45 ppm for C6, and a doublet of doublet peaks corresponding to C7 positioned protons.

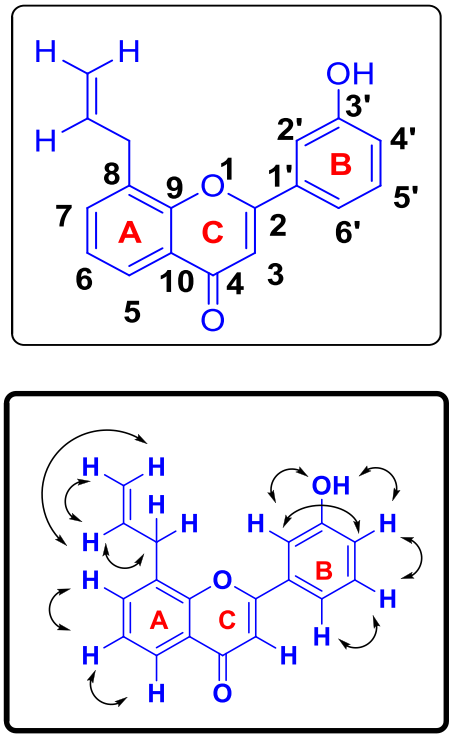
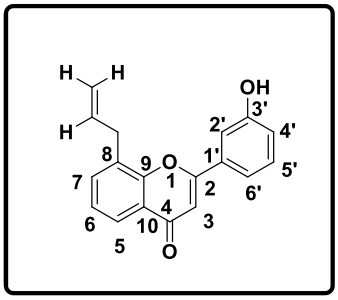


Fig. 2. (8-allyl-2-(3-hydroxyphenyl)-4H-chromen-4-one)

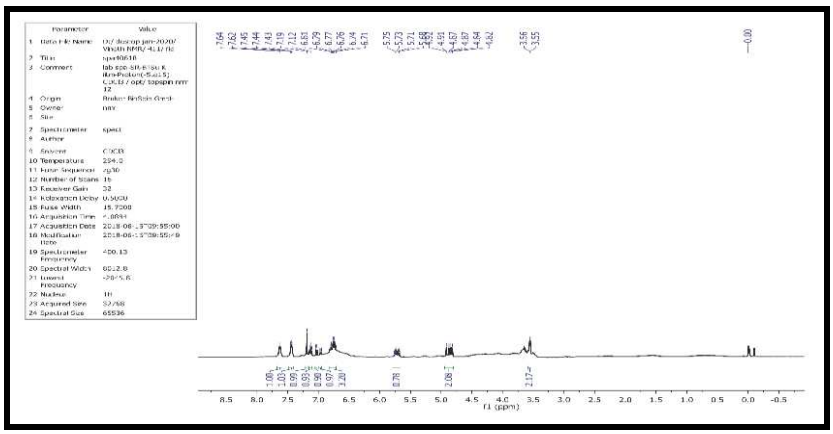
The 13C NMR spectrum (Figure 3b) illustrates several distinctive peaks associated with various carbon environments. Aliphatic -CH2 methylene carbon is observed at 47.81 ppm, while =CH2 alkene carbon appears at 114.07 ppm. The aliphatic allylic methine carbon resonates at 135.14 ppm, and the carbonyl (-C=O) carbon at C4 is detected at 176.70 ppm. Aromatic methine carbons in ring A (C5, C6, and C7) are associated with peaks at 128.84, 130.90, and 123.93 ppm, respectively. In ring B, carbon peaks for C2', C4', C5', and C6' are observed at 123.42, 120.23, 129.53, and 115.32 ppm, respectively. The C3-positioned carbon in ring C is identified at 105.83 ppm.

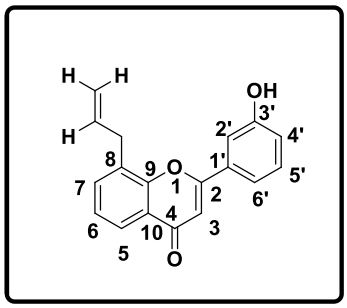
DEPT 135 spectral analysis (Figure 4a) further corroborates the carbon assignments, revealing two secondary carbons (CH2), one tertiary carbon (CH) in the aliphatic region, and eight methine carbons in the aromatic region. Quaternary carbons C2, C8, C9, C10, C1', and C3' are observed at 167.79, 135.14, 157.38, 125.22, 131.10, and 159.46 ppm, respectively. The 2D NMR spectra (Figure 4b), particularly the 1H-1H COSY, offer valuable insights into scalar coupling between adjacent protons, facilitating the assignment of proton environments. The HSQC experiment (Figure 4c) confirms coupling between carbons and protons, thereby clarifying details of molecular connectivity.

Figure 3. (A) 1 H NMR spectral analysis and (B) 13C NMR spectral analysis of Compound (8-allyl-2-(3-hydroxyphenyl)-4H-chromen-4-one).



3A





3B

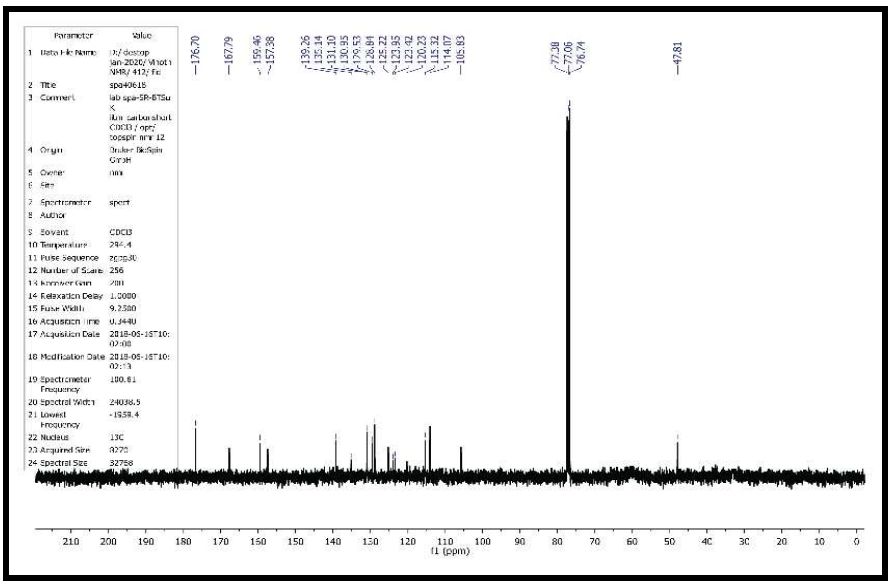
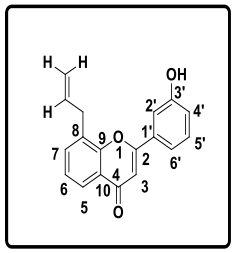
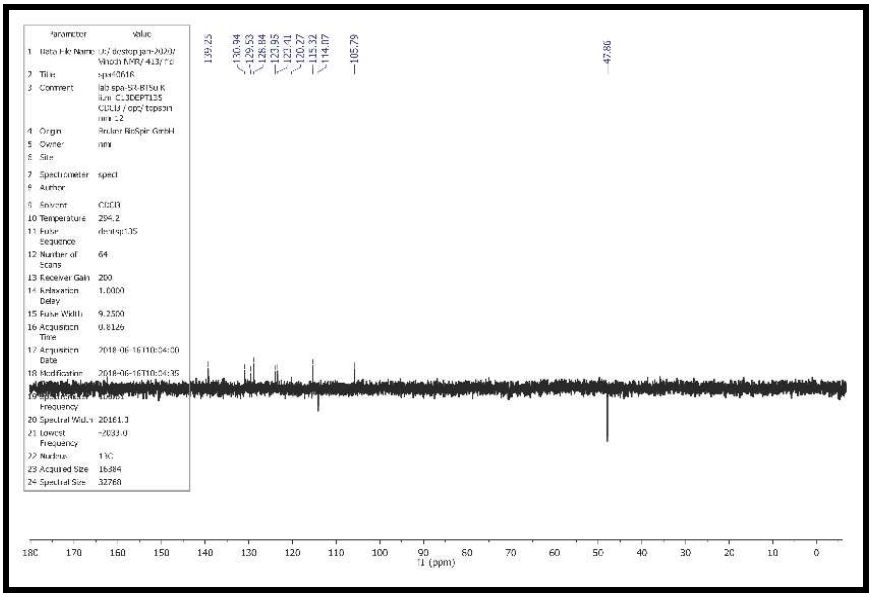
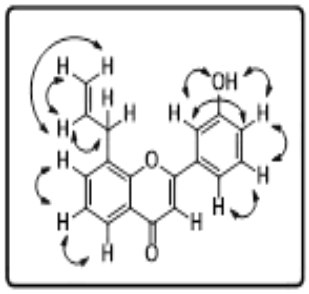


Figure 4. (A) DEPT 135 NMR Spectrum, (B) 1H-1H Cosy NMR Spectrum, and (C) HSQC NMR Spectrum of Compound (8-allyl-2-(3-hydroxyphenyl)-4H-chromen-4-one).

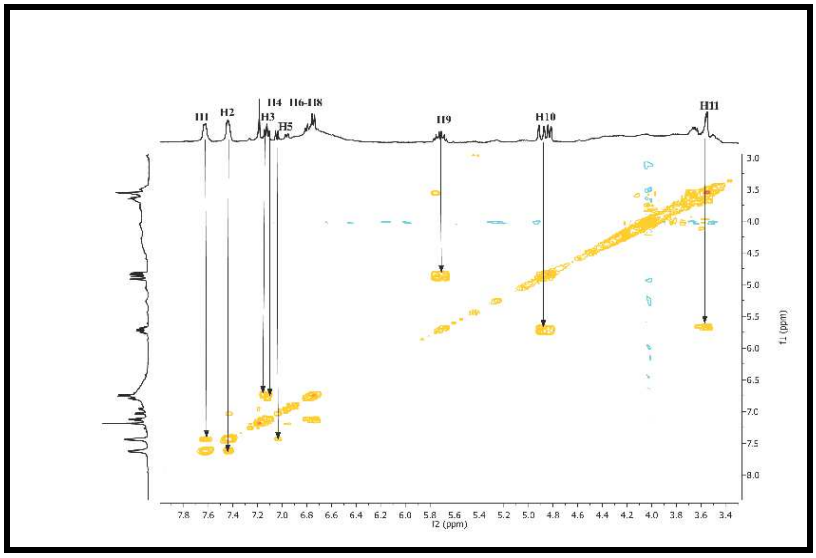


4 A

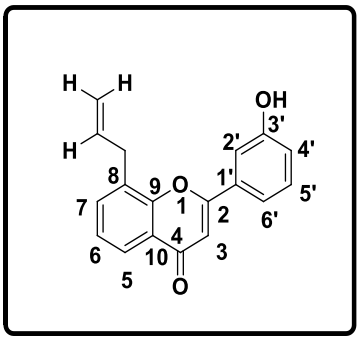




4 B



4 C



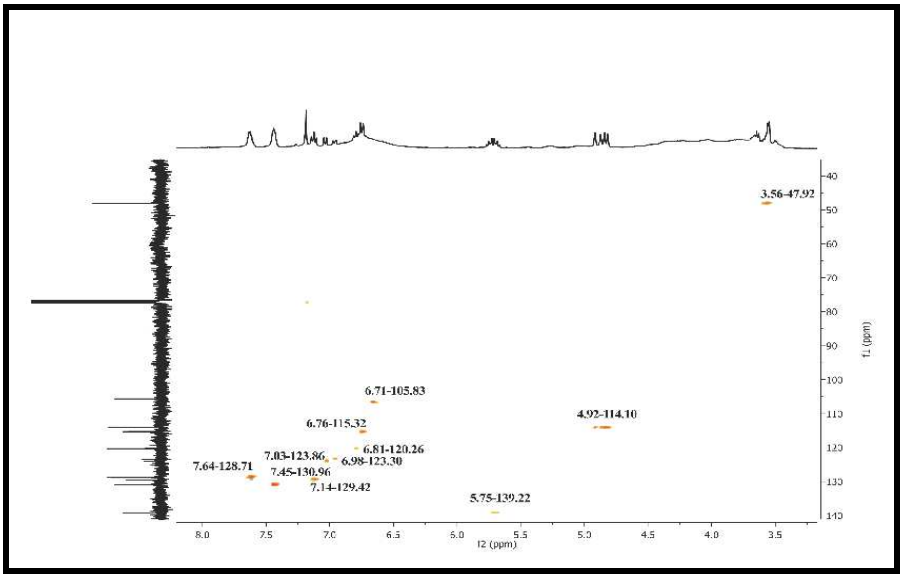
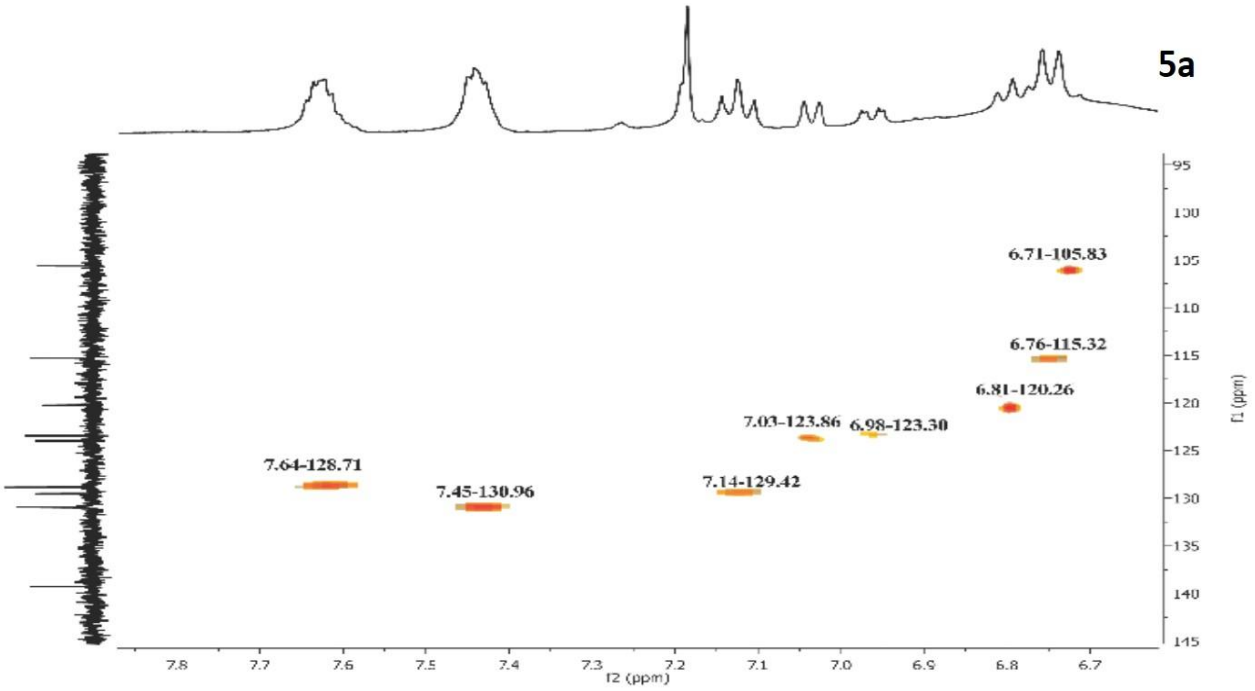


Figure 5 A, B. Mass Spectrum of Compound (8-allyl-2-(3-hydroxyphenyl)-4*H*-chromen-4-one)



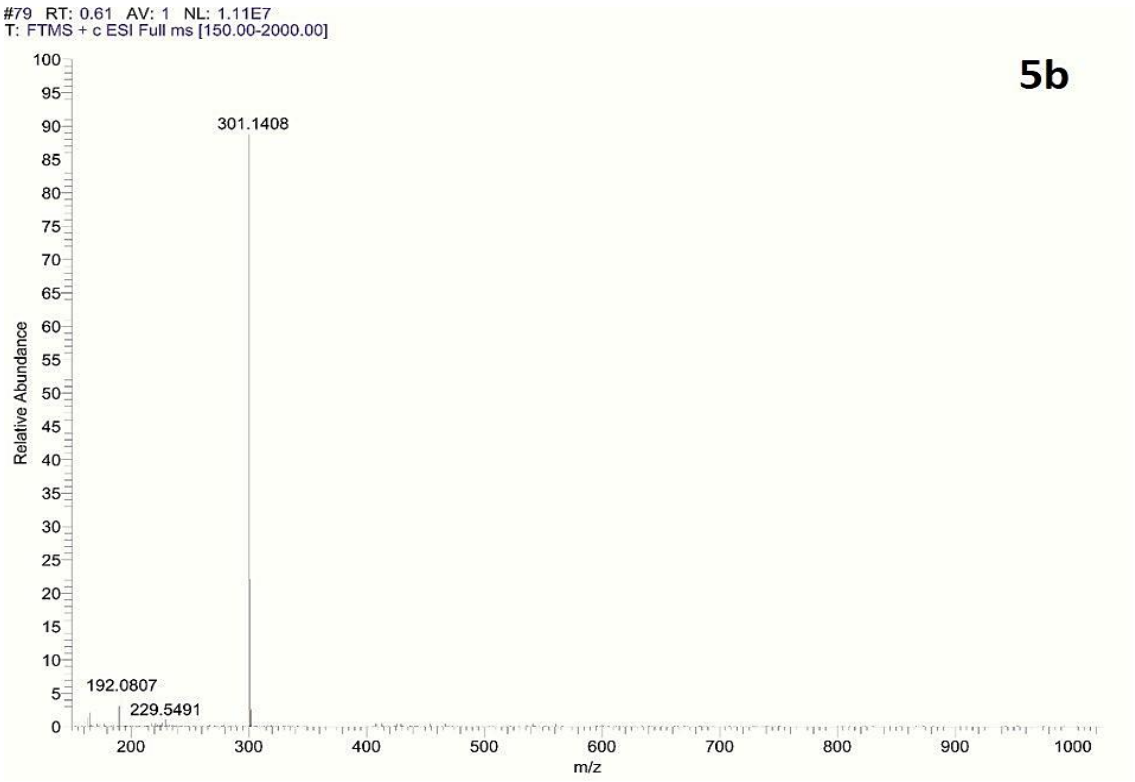


Table 2. 1D and 2D spectral data for (8-allyl-2-(3-hydroxyphenyl)-4*H*-chromen-4-one) compound

Carbon	**δ (^{13}C)**	**δ (^{1}H)**	**δ**	**δ (^{1}H-**	**δ**

Position			(DEPT135)	^{1}HCOSY)	(HSQC(^{1}J))
C3	105.83[b]	6.71 (s, 1H)	107.83(CH)		6.71-105.83
C5	128.84[b]	7.64 (d, *J*=10.0Hz, 1H)	128.84(CH)	7.64-7.45	7.64-128.71
C6	130.90[b]	7.45 (t, *J*=5.0Hz, 1H)	130.94(CH)	7.45-7.64, 7.03	7.45-130.96
C7	123.95[b]	7.03 (dd, $J_{1,2}$=5.0,10.0Hz, 1H)	123.95(CH)	7.03-7.45	7.03-123.86
C2'	123.42[b]	6.98 (dd, $J_{1,2}$=5.0,10.0Hz, 1H)	123.41(CH)	7.25-7.45	6.98-123.30
C3'	159.46[d]	7.18 (s, 1H)	124.41(CH)	6.64-6.45	7.18-159.46
C4'	120.23[b]	6.81 (t, *J*=10.0Hz, 1H)	120.27(CH)	6.81-7.14	6.81-120.26
C5'	129.53[b]	7.14 (t, *J*=10.0Hz, 1H)	129.53(CH)	7.14-6.76, 6.81	7.14-129.42
C6'	115.32[b]	6.76 (d, *J*=10.0Hz, 1H)	115.32(CH)	6.76-7.14	6.76-115.32
Allyl CH	139.26[b]	5.75-5.68 (m, 1H)	139.25(CH)	5.71-4.92, 3.56	5.75-139.22
Alkene CH_2	114.07[a]	4.92-4.82 (m, 2H)	114.07(CH_2)	4.92-5.71	4.92-114.10
Allyl CH_2	47.81[a]	3.56 (d, *J*=5.0Hz, 2H)	47.81 (CH_2)	5.56-5.71	3.56-47.92

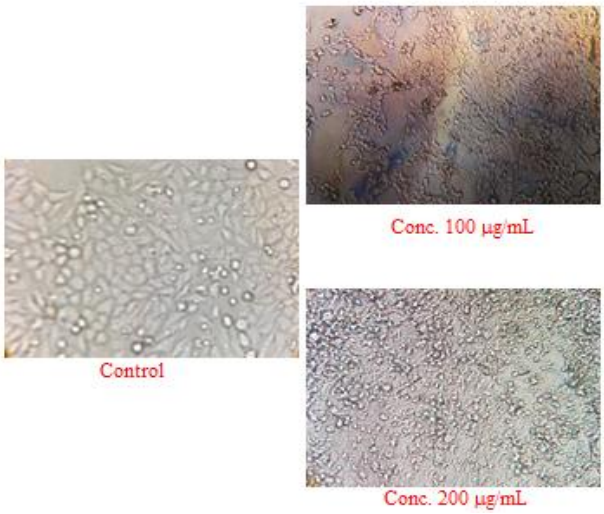
In summary, the spectroscopic analysis of the compound, designated as 8-allyl-2-(3-hydroxyphenyl)-4H-chromen-4-one, is comprehensive and provides valuable structural information. A positive molecular ion [M+Na]+ at m/z=301 further supports the proposed molecular structure, as depicted in Figures 5a and 5b. All spectral data are systematically presented in Table 2.

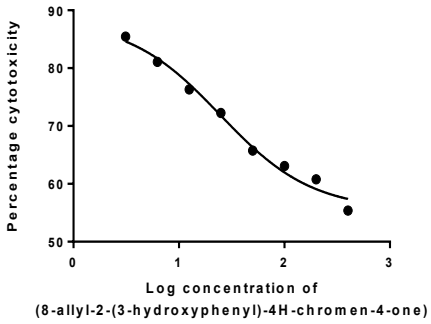
A mass spectrometry analysis showed that the compound's empirical formula (Figure 2, 3, 4, 5,) (8-allyl-2-(3-hydroxyphenyl)-4H-chromen-4-one) is $C_{18}H_{14}O_3$**.**

3.3 Cytotoxicity

Cytotoxicity was observed in HEp G cell lines after 48 hours of treatment with varying test sample concentrations. Also, higher drug concentrations correlated with heightened cytotoxicity towards the HEp G cell lines, as illustrated in Figure 6. The methanol extract demonstrated an IC50 value of 24.70 µg/mL against HEp G cell lines. In vitro cytotoxicity investigations unveiled the susceptibility of the HEp G cell line to cytotoxic effects upon exposure to the test extract, as detailed in the graph.

Fig 6. *In vitro* cytotoxicity effect of (8-allyl-2-(3-hydroxyphenyl)-4H-chromen-4-one) against HEp G cell line.





Sample Concentrations (µg/ml)	HEpG Cell Viability (%)
0	100.00
3.125	85.46
6.25	81.09
12.5	76.32
25	72.25
50	65.75
100	63.10
200	60.77
400	55.38
IC_{50}	24.70

3.4 Screening of Antifungal and Antibacterial Activity of Chromenone Derivatives

As shown in Table 3a, the methanol extract demonstrated notable antibacterial efficacy against various pathogens, including *S. typhi, Bacillus, S. aureus, S. epidermis, Proteus, and E. coli*. However, comparatively lower antibacterial activity was observed against E. coli and S. epidermis species. Importantly, an increase in extract concentration was associated with an augmentation in the zone of inhibition, emphasizing the concentration-dependent nature of the extract's antibacterial activity. Remarkably, at a concentration of 80 µg, the methanol extract displayed potent inhibition against *S. aureus, Proteus, S. typhi, and Bacillus*, yielding zone diameters of 30, 29, and 35 mm, respectively. Notably, although the inhibition zones (ranging from 20-30 mm) produced by each extract against all tested bacteria were smaller than those generated by ampicillin, they still demonstrated significant antibacterial activity and efficacy.

Additionally, Table 4b highlights the extract's antifungal activity against *Candida albicans*, exhibiting substantial inhibition zones indicative of its effectiveness against fungal pathogens.

Table 3a. Zone of inhibition of *Acacia nilotica* leaf methanol extract

MICROORGANISMS	LEAF METHANOL EXTRACT ZONE OF INHIBITION IN mm	AMPICILLIN [POSITIVE CONTROL]
Staphylococcus aureus	15	14
Bacillus subtilis	13	16
Escherichia coli	14	12
Proteus vulgaris	10	11
Staphylococcus epidermis	12	14
Salmonella typhi	13	15

Table 4b. Antifungal activity of *acacia nilotica* leaf methanol extract against fungal organisms

MICRO ORGANISMS	LEAF METHANOL EXTRACT ZONE OF INHIBITION IN mm	FLUCONAZOLE [POSITIVE CONTROL]
Aspergillus niger	11	19
Candida albicans	12	15

3.5 Minimum inhibitory concentration

The materials underwent serial dilution and were subsequently screened against various microorganisms, as outlined in Table 5. The minimum inhibitory concentration (MIC) was determined for each tube, with distinct concentrations observed as bacterial growth progressed. MIC was defined as the lowest sample concentration at which bacterial growth was impaired compared to the increase observed in the control tube. Acacia nilotica was particularly potent against *S. aureus*, *Bacillus subtilis*, *S. epidermis*, and *Proteus vulgaris*.

Table 5. OD Value for Minimal Inhibitory Concentration of *Acacia nilotica* Leaf extract

Microorganism	10^1	10^2	10^3	10^4	10^5	10^6	10^7
Staphylococcus aureus	0.50	0.52	0.62	0.98	1.28	1.49	0.61

Bacillus subtilis	1.03	1.57	1.30	0.85	0.66	0.48	0.75
Escherichia coli	0.65	0.77	0.79	0.96	1.12	1.48	0.99
Proteus vulgaris	0.54	0.68	0.70	0.73	0.82	0.91	0.99
Staphylococcus epidermis	0.94	1.12	0.91	0.65	0.61	0.57	0.62
Salmonella typhi	0.60	1.03	0.65	0.70	0.68	1.32	0.80

3.6 DFT

The theoretical calculations reveal that the studied molecule contains 81 occupied molecular orbitals, and the energy levels along with the spatial distributions of the HOMO, HOMO−1, LUMO, and LUMO+1 orbitals are presented in Fig. 7. In the Chromen-4-one derivative, the HOMO is primarily localized over the chromen-4-one framework and the hydroxyl-substituted phenyl ring, indicating electron density concentration in these regions. In contrast, the LUMO is distributed across almost the entire molecular structure, suggesting its ability to accept electrons over a wider region of the molecule. The frontier molecular orbital energies are important parameters for evaluating several global chemical reactivity descriptors such as chemical hardness (η), chemical potential (μ), softness (S), electronegativity (χ), and electrophilicity index (ω). The values of EHOMO and ELUMO were estimated using Koopmans' theorem. According to this approach, the ionization potential (I) and electron affinity (A) can be expressed as $I = -E_{HOMO}$ and $A = -E_{LUMO}$. Based on these values, the chemical hardness (η) and chemical potential (μ) are determined using the relations $\eta = (I - A)/2$ and $\mu = -(I + A)/2$, which can also be written as $\eta = (-E_{HOMO} + E_{LUMO})/2$ and $\mu = (E_{HOMO} + E_{LUMO})/2$. Furthermore, electronegativity (χ) and the electrophilicity index (ω) are calculated using $\chi = (I + A)/2$ and $\omega = \mu^2/2\eta$. Among these descriptors, chemical potential describes the tendency of a molecule to gain or lose electrons, whereas chemical hardness is related to the resistance of the molecule toward charge transfer and therefore reflects molecular stability. For the investigated compound, the calculated EHOMO and ELUMO values are −6.6091 eV and −2.1606 eV, respectively, giving a HOMO–LUMO energy gap of 4.4485 eV. The corresponding ionization potential (I) and electron affinity (A) are −6.6091 eV and −2.1606 eV. The calculated global hardness (η) is 2.2243 eV, while the chemical potential (μ) is −4.3848 eV, and the electrophilicity index (ω) is 4.3822 eV. The negative value of chemical potential indicates that the Chromen-4-one compound possesses good thermodynamic stability. Generally, hard molecular systems are smaller and less polarizable, whereas soft systems tend to be larger and more polarizable. The electrophilicity index represents the stabilization energy obtained when electrons are transferred between donor and acceptor species. The calculated frontier molecular orbital parameters of the Chromen-4-one compound are summarized in Tables 6 and 7.

3.7 Molecular electrostatic potential analysis

The molecular electrostatic potential (MEP) surface illustrates the three-dimensional distribution of electrostatic charge over a molecule. Analysis of the MEP surface helps in identifying reactive regions and understanding the possible biological behavior of a compound. The electrostatic potential surface calculated for the DMPC molecule is presented in Fig. 8. The generated 3D MEP map shows that the negative potential region, represented by red color, is mainly located near the carbonyl group of the Chromen-4-one ring, suggesting this area as a probable electrophilic interaction site. The positive

potential region, indicated by blue color, appears around the hydrogen atom of the hydroxyl group attached to the phenyl ring, pointing to a region favorable for nucleophilic interactions. Areas shown in green correspond to nearly neutral electrostatic potential. These observations suggest that the molecule may participate in both intra- and intermolecular interactions in the solid state, as depicted in Fig. 9.

3.8 Optimized molecular geometry

Quantum chemical calculations for Chromen-4-one compound has been carried out at the B3LYP level of theory with the 6-311++G (d,p) basis set using the Gaussian 09 program package. The initial geometry, derived from geometric parameters, was optimized at the DFT level without any constraints. The energy of the chromen-4-one compound has been calculated as -920.2448 a.u and its dipole moment also calculated as 5.0934 Debye. The optimized molecular structure of Chromen-4-one compound has shown in Fig. 9. The frontier molecular orbital analysis and the molecular electrostatic potential (MEP) mapped surface of the Chromen-4-one compound were also calculated using the same level of theory with the Gaussian package.

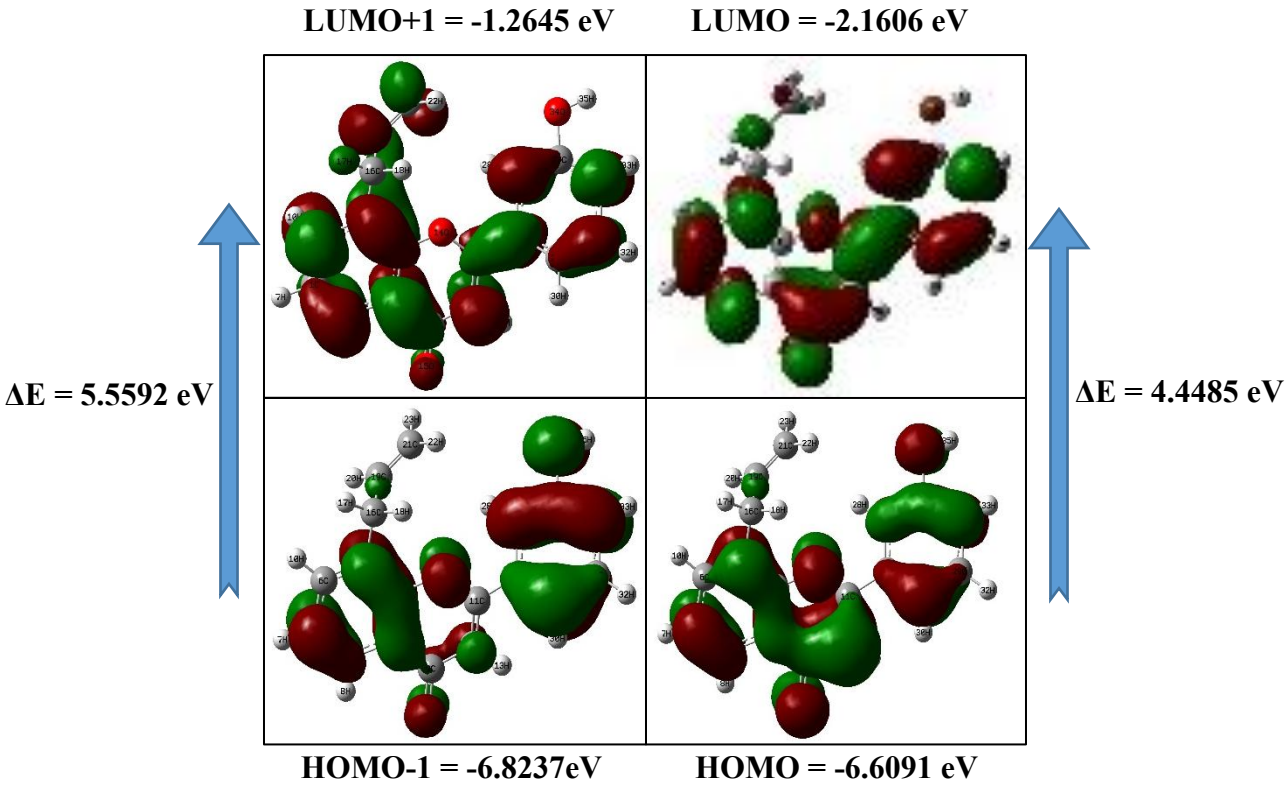


Fig.7 The HOMO and LUMO mapped surfaces of Chromen-4-one compound

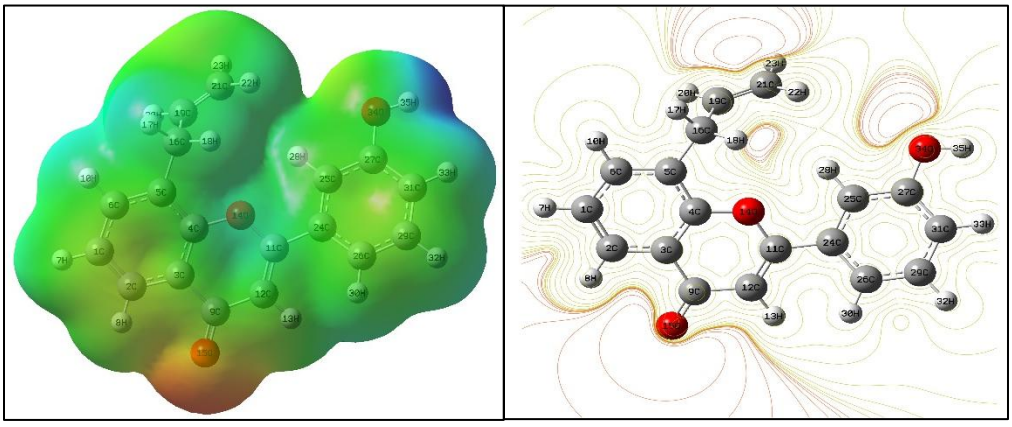


Fig. 8 The molecular electrostatic potential mapped surface and 2D-contour mapped surface of Chromen-4-one compound.

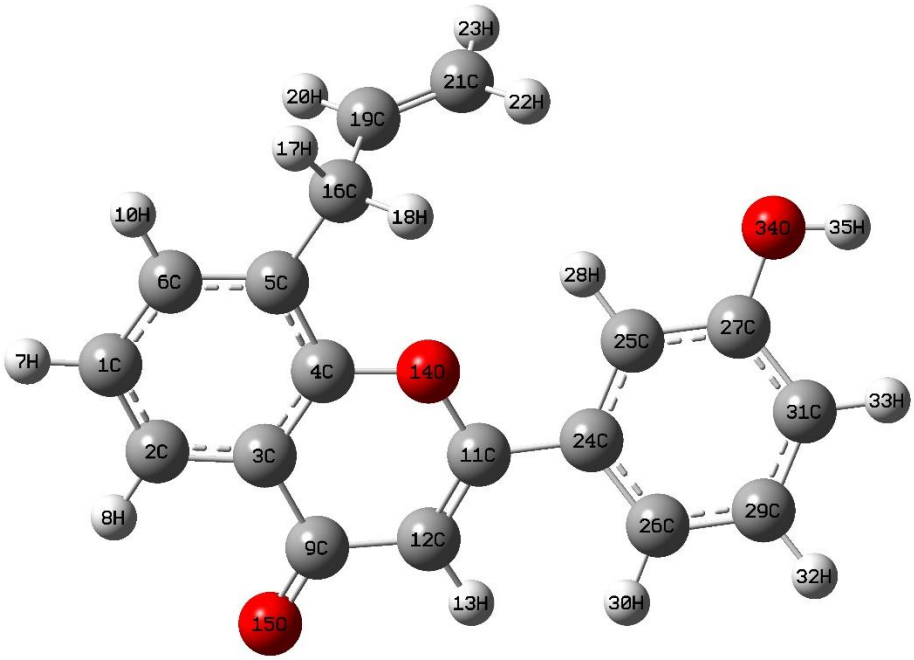


Fig. 9 The optimized molecular structure of Chromen-4-one compound at DFT level.

Table 6 The energy gap analysis of Chromen-4-one

Orbitals	**Energies (a.u)**	**Energies (eV)**	**Kinetic energy**
69O	-0.2673	-7.2735	1.3270
70O	-0.2633	-7.1635	1.2921
71O	-0.2527	-6.8774	1.9981
72O	-0.2508	-6.8237	1.8576
73O	-0.2429	-6.6091	1.5851
74V	-0.0794	-2.1606	1.5805
75V	-0.0465	-1.2645	1.3482

76V	-0.0267	-0.7271	1.3304
77V	-0.0225	-0.6111	0.3976
78V	-0.0201	-0.5472	1.4331

Table 7 The global reactivity descriptors of Chromen-4-one

Global reactivity descriptors	**Energies (eV)**
E_{HOMO} (Ionization potential I)	6.6091
E_{LUMO} (Electron affinity A)	2.1606
E_{HOMO-1}	6.8237
E_{LUMO+1}	1
$(E_{HOMO} - E_{LUMO})$ gap	4.4485
$(E_{HOMO-1} - E_{LUMO+1})$ gap	5.5592
Chemical potential (μ)	-4.3848
Chemical hardness (η)	2.2243
Chemical softness (S)	0.4496
Electrophilicity index (ω)	4.3822
Nucleophilicity	0.0468
Electronegativity	4.3849

3.9 3D structure modeling and protein-ligand interaction

The 3D structure of the cancer protein was elucidated using the SWISSMODEL server with the template PDB ID: 8I0L (Structure of CDK9/cyclin T1 in Complex with Inhibitor). The 3D model that showed the highest GMQE score (0.92) and QMEAN Z-score (0.86 ± 0.05) was considered the best protein model structure for the protein-ligand study. Molecular docking of the protein-ligand complex revealed that the molecule had a considerably good binding affinity score of -10.3 kcal/mol. The results indicated that the compound's protein-ligand interaction is visualized and represented in Fig. 10. The docking results further showed that compound 8-allyl-2-(3-hydroxyphenyl)-4H-chromen-4-one interacted with the active site residue CDK9 Fig. 10, and the surface model of the best binding pose of the compound in CDK9 is shown in Fig. 11

Fig 10: Binding interactions 8-allyl-2-(3-hydroxyphenyl)-4H-chromen-4-one compound in the active site of CDK9

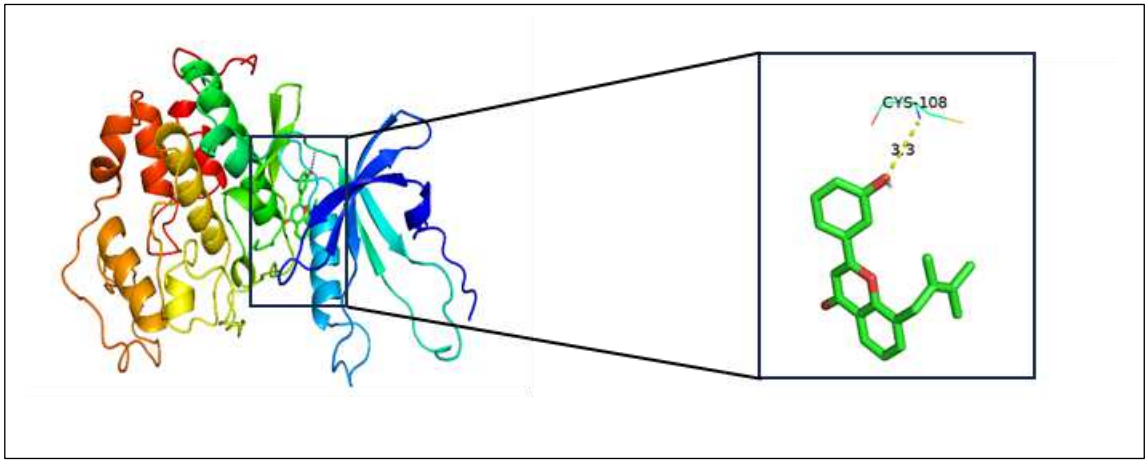
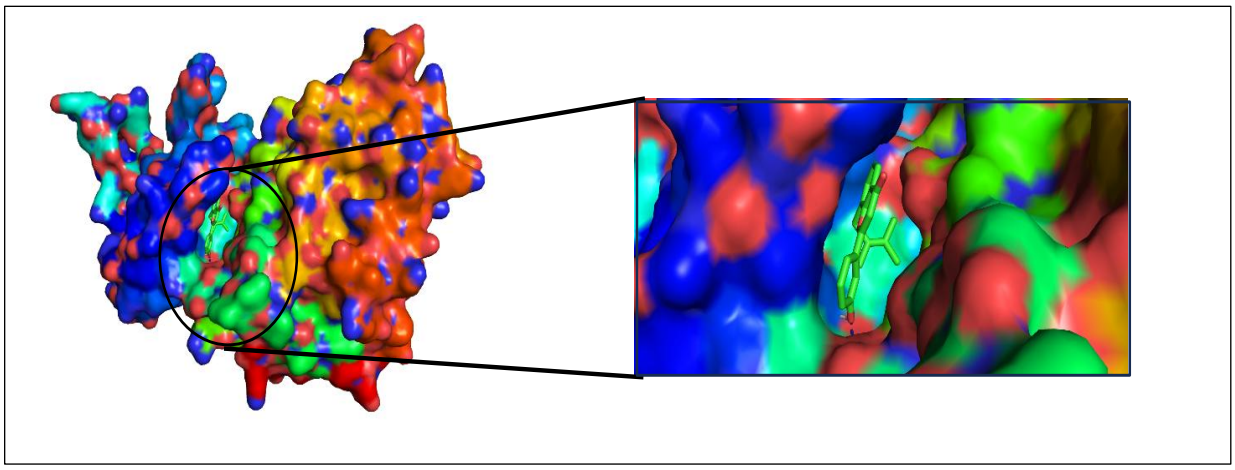


Fig 11: Binding orientation of 8-allyl-2-(3-hydroxyphenyl)-4H-chromen-4-one compound in the active site of CDK9



3.10 Molecular Dynamics Investigation of the Complex

Molecular dynamics simulation is widely used to understand the structural mechanisms and functional dynamics of biomolecular systems. In this study, the molecular dynamics simulation of the 8-allyl-2-(3-hydroxyphenyl)-4H-chromen-4-one–CKD9 complex was carried out for a period of 100 ns. The root mean square deviation (RMSD) was calculated to examine the conformational stability and structural changes of the backbone atoms of the complex, and the RMSD plot is presented in Fig. 12A. The system showed an increase in stability during the initial 40 ns of the simulation and later maintained a stable pattern with minor fluctuations around 2.5 Å. The root mean square fluctuation (RMSF) analysis was performed to evaluate the flexibility of individual amino acid residues in the protein–ligand complex. RMSF measures the deviation of each alpha carbon atom from its average position during the simulation, and the distribution of residue flexibility in the complex is shown in Fig. 13B. Higher RMSF values indicate flexible regions in the structure, whereas lower values suggest stable and well-maintained secondary structural elements. The intermolecular hydrogen bonding interactions between 8-allyl-2-(3-hydroxyphenyl)-4H-chromen-4-one and CKD9 were also analysed, and the variation in the number of hydrogen bonds during the simulation is presented in Fig. 14C. The results revealed the formation of three hydrogen bonds, indicating stable binding between the ligand and the protein

throughout the simulation. In addition, the radius of gyration (Rg) was calculated to determine the compactness of the molecular system. The Rg value reflects the spatial distribution and structural packing of the molecular chain, and the corresponding results are illustrated in Fig. 15D, confirming the compact nature of the complex during the simulation.

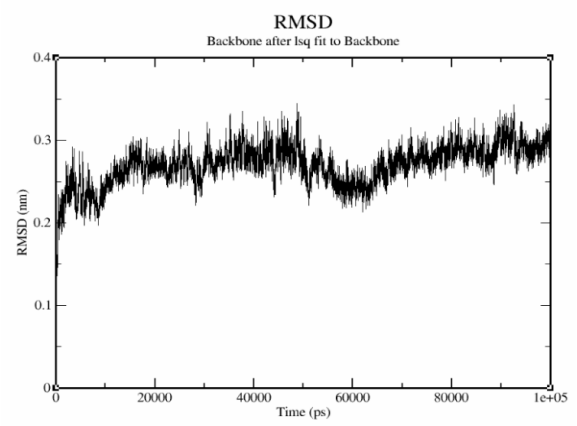


Fig 12A: RMSD graph of chromen-4-one compound

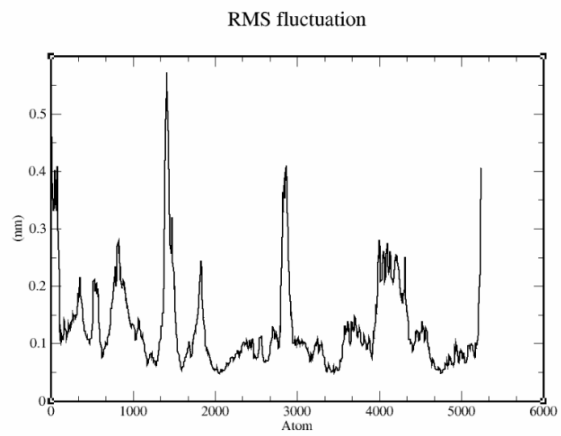


Fig 13B: RMSF of chromen-4-one compound

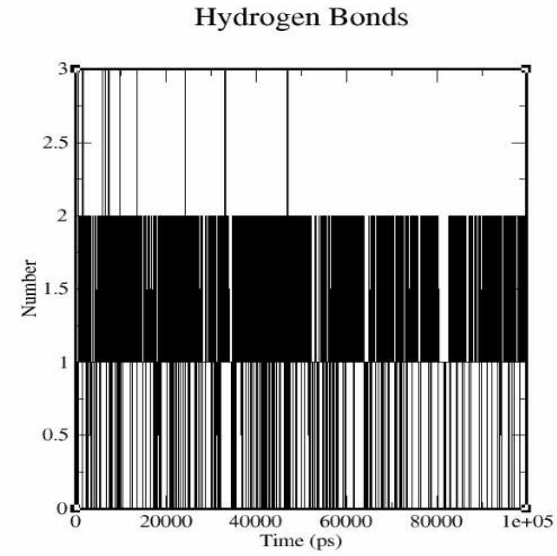


Fig 14C: H bond of chromen-4-one compound

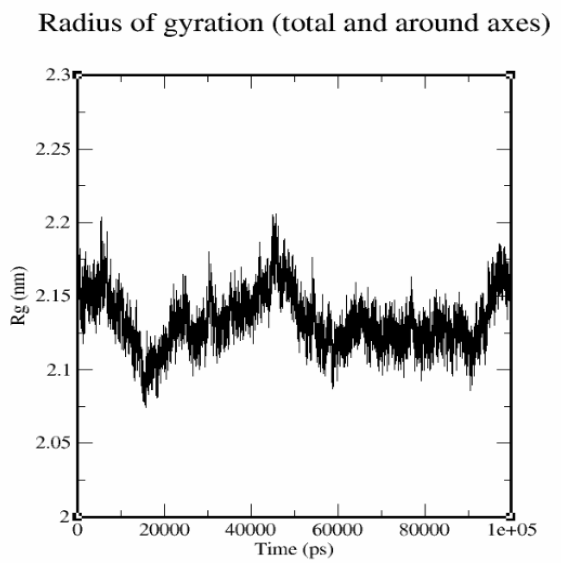


Fig 15D: Radius of Gyration of chromen-4-one compound

3. Conclusion

Our investigation successfully isolated the chromen-4-one derivative compound from the methanol extract of Acacia nilotica leaves and characterized its molecular structure through spectral analyses, yielding a molecular formula of $C_{18}H_{14}O_3$. The compound is identified as (8-allyl-2-(3-hydroxyphenyl)-4H-chromen-4-one). Furthermore, we confirmed that the chromen-4-one compound contains antibacterial properties and demonstrates potent anticancer activity. Finally, our findings stress the importance of future research to explore potential clinical applications of the chromen-4-one derivative compound. DFT analysis confirmed the structural stability and moderate reactivity of the Chromenone compound. The HOMO–LUMO gap and MEP mapping revealed key reactive sites, supporting its potential for molecular docking studies. From *insilico* analysis of molecular docking and

molecular simulation exhibit the high binding affinity -10.3 kcal/mol with three hydrogen bonds between 8-allyl-2-(3-hydroxyphenyl)-4H-chromen-4-one and CKD9 were observed, indicating that a stable binding was formed during the simulation. Moreover, investigations into other natural extracts as possible sources of novel therapeutics for antibacterial and anticancer purposes are warranted. Our study highlights this research avenue's critical role in developing innovative treatment modalities with enhanced efficacy and reduced side effects.

Author Contributions:

MV and PK designed the research. MV and PK performed the experimental work. Data analysis was carried out by AD, KM, The manuscript was prepared by MV PK

Funding:

This study was conducted without any external financial support.

Informed Consent Statement:

Not applicable.

Data Availability Statement:

The datasets generated or analysed during the current study can be obtained from the corresponding author upon reasonable request.

Conflicts of Interest:

The authors declare that there are no conflicts of interest or competing interests related to this work.

References:

1. Ahmed, N., Kandhro, A.A., Chaudhry, A., Shaikh, A.R., Qureshi, A.U., Hayat, A., et al., *Applied Fruit Science*, **66,** 247–255, (2024).
2. Alduraihem, N.S., Bhat, R.S., Al-Zahrani, S.A., Elnagar, D.M., Alobaid, H.M., Daghestani, M.H*, Processes*, **11(2)**, 301, (2023).
3. Ali, A., Akhtar, N., Khan, B.A., Khan, M.S., Rasul, A., Zaman, S.U., et al, *J. Medicinal Plants Research*, **6**, 1492–1496, (2012*)*.
4. Vinoth, M., & Natarajan, B, *International Journal of Research in Pharmaceutical Sciences*, **12(1)**, 1–6, (2021).
5. Altemimi, A., Lakhssassi, N., Baharlouei, A., Watson, D.G., Lightfoot, D.A, *Plants (Basel)*, **6(4)**, 42. (2017).
6. Vinoth, M., Natarajan, B., & Shanmuga Sundaram, C, *Indian Journal of Chemical Technology*, **28(2)**, 188–196, (2021).
7. Arshad, M., Hussain, I., Mahmood, M.S., Khan, M. (2017). *Pakistan Journal of Agricultural Sciences*, **54(2)**, 423–430.
8. Baz, M.M., El-Shourbagy, N.M., Alkhaibari, A.M., Gattan, H.S., Alruhaili, M.H., Selim, A., et al., *Scientific Reports*, **14**, 6248, (2024).
9. Buhari, S.S., Idris, S.L., Saidu, B.M., Namadina, M.M., Galalain, A.M., Yakasai, M.A., et al., *Biological Sciences*, **4(1)**, 525–534. (2024).
10. Chau, T.P., Devanesan, S., Ayub, R., Perumal, K, *Environmental Research*, 242, 117763. (2024).
11. El-Chaghaby, G.A., Rashad, S., El-Sayed, H.G.M., Abdel-Wareth, A.A.A, *SVU-International Journal of Agricultural Sciences*, **6(1)**, 88–97. (2024).
12. Firdhouse, M.J., Lalitha, P, *Journal of Nanotechnology*, **2015**, 829526. (2015).
13. Guta, M., Urga, K., Assefa, A., Lemma, H., Addis, G., Gemeda, N., et al., *Ethiopian Journal of Biological Sciences*, **6(1)**, 43–49. (2009).
14. Vinoth, M., & Natarajan, B, *Rasayan Journal of Chemistry*, **14(2)**, 768–777. (2021).
15. Konappa, N., Udayashankar, A.C., Krishnamurthy, S., Pradeep, C.K., Chowdappa, S., Jogaiah, S., *Scientific Reports*, **10(1)**, 16438. (2020).
16. Kumar, Y., Wani, F.A., Ahmedi, S., Shamsi, A., Nadeem, M., Manzoor, N., et al., *Journal of Molecular Liquids*, **401**, 124631. (2024).
17. Mothana, R.A., Lindequist, U., Gruenert, R., Bednarski P.J., *BMC Complementary and Alternative Medicine*, **9(7),** 1472-6882, (2009).
18. Murugan, J.M., Ramkumar, G., Mwang'onde, B.J., Thomas, A., Mihale, M.J., Muthusamy, R., et al., *Journal of Natural Pest Research*, **7**, 100062. (2024).
19. Okoro, S., Kawo, A.H., Arzai, A. , *Journal of Pure and Applied Sciences*, **5(1)**, 163–170. (2012).
20. Ramachandran V, Arumugasamy K, Singh SK, Edayadulla N, Ramesh P, Kamaraj SK. *J Chem Biol,* **9(1)**, 31-40. (2015).
21. Rauf, A., Ibrahim, M., Alomar, T.S., AlMasoud, N., Khalil, A.A., Khan, M., et al.. *Food Science & Nutrition,* **00**, 1–9, (2024).
22. Sadiq, M.B., Tarning, J., Aye Cho, T.Z., Anal, A.K.,*Molecules,* **22(1)**, 47. (2017).
23. Samy, R.P., Gopalakrishnakone, P., *Evidence-Based Complementary and Alternative Medicine*, **7(3)**, 283–294. (2010).
24. Shehata, M.E., El-Sherbiny, G.M., Sharaf, M.H., Kalaba, M.H., Shaban, A.S., *Biomass Conversion and Biorefinery*, **(15),** 3753–3770, (2024).

25. Subhan, N., Burrows, G.E., Kerr, P.G., Obied, H.K., *Studies in Natural Products Chemistry* **57**, 247–326, (2018).
26. Zhang, X.F., Liu, Z.G., Shen, W., Gurunathan, S., *International Journal of Molecular Sciences*, **17(9)**, 1534. (2016).
27. *Seebach, D. Frontier Orbitals and Organic Chemical Reactions. Von I. Fleming. John Wiley & Sons, London*, *2010.*
28. M. Uthayakumar, A. P. Jeyakumari, A. Dhandapani, V. Shinde, and M. Arivanandhan, *J. Phys. D: Appl. Phys.,* **52**, 39, 395102. (2019).
29. *M. J. Frisch, G. W. Trucks, H. B. Schlegel, G. E. Scuseria, M. A. Robb, J. R. Cheeseman, G. Scalmani, V. Barone, B. Mennucci, G. A. Petersson, et al., Gaussian 09, Revision D.01, Gaussian, Inc., Wallingford CT, 2013*.
30. Waterhouse, A., Bertoni, M., Bienert, S., Studer, G., Tauriello, G., Gumienny, R., et al., *Nucleic Acids Research*, **46(1)**, 296–303. (2018).
31. Vinoth, M., & Natarajan, B.. Rasayan, *Journal of Chemistry*, **14(3)**, 1667–1679. (2021).
32. Swetha TK, Pooranachithra M, Subramenium GA, Divya V, Balamurugan K, Pandian SK., *Front Cell Infect Microbiol,***9**,357, 2019.
33. Trott, O., Olson, A.J., *Journal of Computational Chemistry*, **31(2)**, 455–461, (2010).
34. Abraham, M.J., Murtola, T., Schulz, R., Páll, S., Smith, J.C., Hess, B., Lindahl, E.*, SoftwareX*, **1–2**, 19–25, (2015).
35. Van Der Spoel, D., Lindahl, E., Hess, B., Groenhof, G., Mark, A.E., Berendsen, H.J.C., *Journal of Computational Chemistry*, **26(16)**, 1701–1718, (2005).
36. Vinoth, M., et al. (2024). Molecular docking studies of Pisonia grandis against herpes simplex virus:Insights from computational analysis. In: Proceedings of the Third International Conference on Smart Technologies and Systems for Next Generation Computing (ICSTSN) 1–4. IEEE.
37. Alyahya SA, Govindarajan M, Alharbi NS, Kadaikunnan S, Khaled JM, Mothana RA, Al-Anbr MN, Vaseeharan B, Ishwarya R, Yazhiniprabha M, Benelli G. J Photochem Photobiol B, **181**,70-79, 2018.
38. Buck, M., Bouguet-Bonnet, S., Pastor, R.W., MacKerell, A.D. Biophysical Journal, **90(4)**. (2006).
39. Hollingsworth, S.A., Dror, R.O., *Molecular dynamics simulation for all.* Neuron, **99(6)**, 1129–1143. (2018).

Figure 1 FTIR analysis of chrome-4 one derivative compound 4
Figure 2 Structural elucidation of (8-allyl-2-(3-hydroxyphenyl)-4H-chromen-4-one)
Figure 3a 1 H NMR spectral analysis of compound (8-ally-2-(3-hydroxyphenyl)-4H-chrome-4-one)
Figure 3b 13C NMR spectral analysis of Compound (8-ally-2-(3-hydroxyphenyl)-4H-chrome-4-one)
Figure 4a DEPT 135 NMR Spectrum of Compound (8-allyl-2-(3-hydroxyphenyl)-4H-chromen-4-one).
Figure 4b 1H-1H Cosy NMR Spectrum of Compound (8-allyl-2-(3-hydroxyphenyl)-4H-chromen-4-one).
Figure 4c HSQC NMR Spectrum of Compound (8-allyl-2-(3-hydroxyphenyl)-4H-chromen-4-one).
Figure 5a Mass Spectrum of Compound (8-allyl-2-(3-hydroxyphenyl)-4*H*-chromen-4-one)

Figure 5b Mass Spectrum of Compound (8-allyl-2-(3-hydroxyphenyl)-4*H*-chromen-4-one)
Figure 6 In vitro cytotoxicity effect of (8-allyl-2-(3-hydroxyphenyl)-4H-chromen-4-one) against HEp G cell line.
Figure 7 The HOMO and LUMO mapped surfaces of the Chromen-4-one compound
Figure 8 The molecular electrostatic potential mapped surface and the 2D-contour mapped surface of Chromen-4-one compound.
Figure 9 The optimized molecular structure of Chromen-4-one compound at the DFT level.
Figure 10 Binding interactions 8-allyl-2-(3-hydroxyphenyl)-4H-chromen-4-one compound in the active site of CDK9
Figure 11 Binding orientation of 8-allyl-2-(3-hydroxyphenyl)-4H-chromen-4-one compound in the active site of CDK9
Figure 12 RMSD graph of chromen-4-one compound
Figure 13 RMSF of chromen-4-one compound
Figure 14 H bond of chromen-4-one compound
Figure 15 Radius of Gyration of chromen-4-one compound